This is an *Accepted Manuscript*, which has been through the Royal Society of Chemistry peer review process and has been accepted for publication.

*Accepted Manuscripts* are published online shortly after acceptance, before technical editing, formatting and proof reading. Using this free service, authors can make their results available to the community, in citable form, before we publish the edited article. We will replace this *Accepted Manuscript* with the edited and formatted *Advance Article* as soon as it is available.

You can find more information about *Accepted Manuscripts* in the **Information for Authors**.

# Chemical Communications

## COMMUNICATION

# Morphology controlled synthesis of monodispersed manganese sulfide nanocrystals and their primary application for supercapacitor with high performance

Yongfu Tang*, Teng Chen, Shengxue Yu
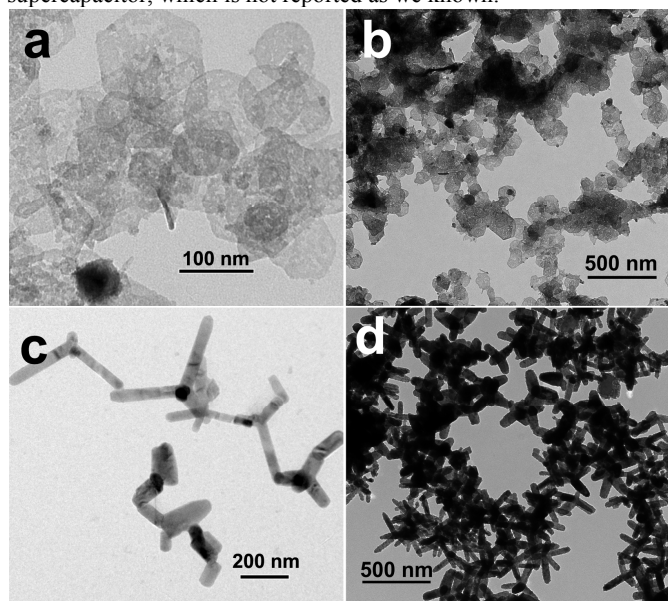
**Monodispersed hollow spindle-like nanospheres (HS-NSs) and tetrapod nanorods (TP-NRs) MnS nanocrystals are obtained via a facile template-free hydrothermal process. The MnS nanocrystals are primary used as supercapacitor materials and exhibit high performance. The TP-NRs nanocrystals show higher specific capacitance of 704.5 F g$^{-1}$ than that of HS-NSs nanocrystals, both of which are higher than that of manganese oxide.**

As a typical semiconductor material, manganese sulfide (MnS) nanocrystals have been attracting more researchers' attentions in the potential applications for optical material,[1] magnetic devices[2] and catalysis.[3] However, the electrochemical applications of MnS nanocrystals are few reported, although the other manganese based materials, manganese oxides, have been widely used in Zn-Mn batteries,[4] Li-ion batteries,[5] supercapacitors[6, 7] and electrocatalysts.[8] The limited literatures about the electrochemical properties of MnS materials are restrained in the organic electrolytes for lithium-ion batteries[9,10] and lithium-sulfur batteries.[11] To our best known, there are no reports about the electrochemical properties in the aqueous electrolytes for supercapacitors. Based on the rich variable valences of manganese element and the suitable layered structure of hexagonal wurtzite γ-phase MnS nanocrystals for the intercalation of ions to balance the increased valence, the MnS materials should be potentially used in the electrochemical supercapacitors and batteries. Moreover, since cobalt, nickel and their binary sulfides possess much higher electronic conductivity than their oxides,[12, 13] the manganese sulfides should exhibit higher conductivity than manganese oxides, being expected to solve the key challenge (low electronic conductivity) for the application of low-cost manganese oxides in supercapacitor.

Besides, as the materials for supercapacitor, high electrochemical reactivity and suitable structure for ionic transportation are also required. As we known, there are three phases for manganese sulfide:[14-15] green stable α-phase MnS with rock salt structure, pink metastable β-phase MnS with zinc blendle structure and pink metastable γ-phase MnS with wurtzite structure. The expanded interlayer of γ-phase MnS with wurtzite structure, which enhances the kinetics of the intercalation of hydroxyl ion, will

possess high electrochemical reactivity for the capacitive behavior. Various morphologies including polyhedral nanocrystals,[16] tetrapod nanorods,[17] nanowires,[18] have been obtained for MnS nanocrystals. The three dimensional structure with defined porous structure can provide the suitable ionic transportation channels for the electrochemical process in the supercapacitor. Therefore, designing and manipulating the structure, phase and morphology is expected to construct MnS nanocrystals with high performance for supercapacitor, which is not reported as we known.
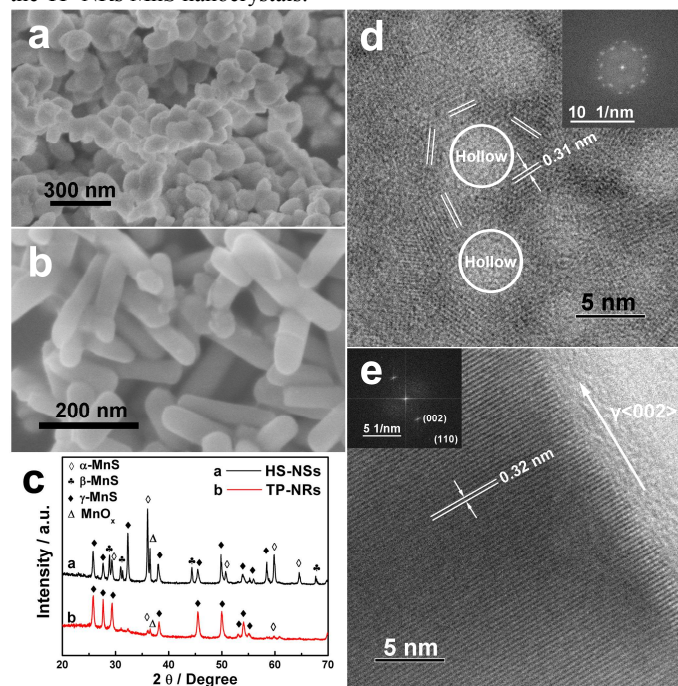


**Figure 1**. High magnified (a) and low magnified (b) TEM images of the HS-NSs MnS nanocrystals, as well as high magnified (c) and low magnified (d) TEM images of the TP-NRs MnS nanocrystals

Herein, monodispersed hollow spindle-like nanospheres (HS-NSs) and tetrapod nanorods (TP-NRs) MnS nanocrystals were obtained via a facile template-free hydrothermal synthesis easily by tuning sulfide ion content with the ammonia as the complex agent and pricipitator. As shown in the TEM image (**Figure 1a**), HS-NSs with the sizes of ~ 100 nm are obtained when the sulfide ion content

is 1.5 mmol. When the sulfide ion content is increased to 3.0 mmol, the product is transferred into monodispersed tetrapod nanorod single crystals (**Figure 1c**). The aspect ratio of the branches is about 5 with the width of 50 nm. The low magnified TEM images of HS-NSs (**Figure 1b**) and TP-NRs MnS nanocrystals (**Figure1d**) demonstrates their good monodispersity.
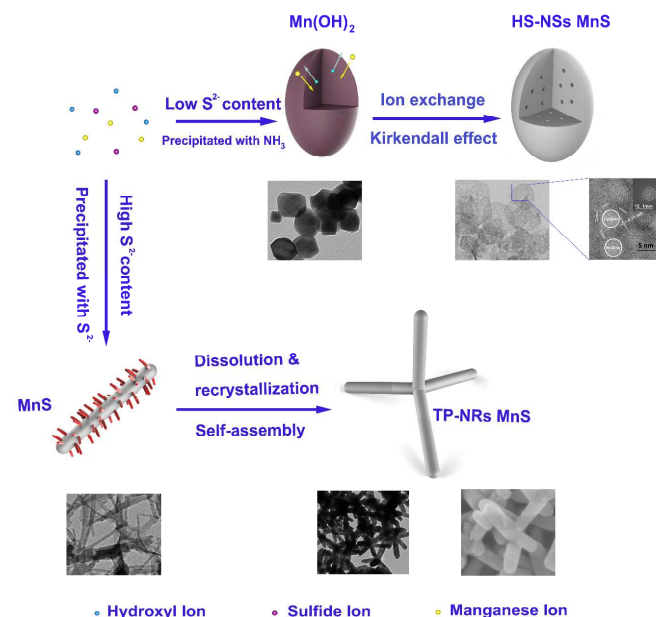
The SEM images of HS-NSs (**Figure 2a**) and TP-NRs (**Figure 2b**) confirm the monodispersity of spindle-like nanospheres and tetrapod nanorods, as well as that the morphology of HS-NSs is the spindle-like nanospheres rather than nanosheets. The XRD pattern (**Figure 2c**) indicates the coexistence of α-phase and γ-phase, together with little β-phase, in the HS-NSs MnS nanocrystals. By contrast, much purer γ-phase MnS is detected in the XRD pattern of TP-NRs nanocrystals. It is also confirmed by the HRTEM images. As shown, the hollow structure in HS-NSs (**Figure 2d**) is an secondary structure, which is constructed by the nanocrystals with different direction similar to Chinese "Octa-Diagram". The interplanar distance is about 0.31 nm, near to those of α(111), β(111), γ(100), γ(002) and γ(101) facets, may be ascribed to any one of these facets. The FFT plots (inset of **Figure 2d**), corresponding to various facets with only small difference, provide the more clear evidence. In another aspect, regular facet with distance of ~ 0.32 nm, corresponding to the (0 0 2) facet of γ-phase, is along with the direction of the nanorod (**Figure 2e**) in TP-NRs MnS. The <0 0 2> direction of the nanorod and the hexagonal wurtzite structure with parallel manganese layer and sulfide layer between (0 0 2) facets will make the oxidation of MnS via the intercalation of hydroxyl ion easily, which can much enhance the electrochemical capacitance of the TP-NRs MnS nanocrystals.

as follows. As shown in **Scheme 1**, with the coexistance of sulfide ion and ammonia in the synthesis, manganese sulfide and manganese hydroxide will form simultaneously. However, with the constant of the ammonia content, solid spindle-like $Mn(OH)_2$ nanospheres are preferentially formed when the sulfide ion content was low (1.5 mmol), which can be confirmed by that solid spindle-like $Mn(OH)_2$ nanocrystals are obtained when only ammonia were used as precipitator (**ESI †**, **Figures S1a** and **S1b**). The MnS nanocrystals are obtained by precipitation transformation via ion exchange due to the lower solubility product of manganese sulfide than that of manganese hydroxide. The formation of hollow nanospheres should be ascribed to the different diffusing rates between the sulfide ion and the hydroxyl ion analogous to Kirkendall effect.[19-21] The evolution of the HS-NSs nanocrystals with the reaction time (size of the hollow pores increase with the increasing of reaction time) also clearly illustrates the Kirkendall effect and the formation of HS-NSs nanocrystals (**Figure S2**). By contrast, when the sulfide ion concentration was high (3.0 mmol), the manganese sulfide nanorods coated by floccules are preferentially formed, which can be verified by that irregular nanorods coated by fluccules are obtained with the absence of ammonia (**Figures S1c and S1d**). With the chemical etching and dissolution-recrystallization of MnS floccules by ammonia via the reaction as **Equations S1** and the structure-directing effect of adsorbed ammonia molecules, regular MnS nanorods are evolved from the floccule coated ones. The nanorods will construct three-dimensional tetrapod structure via self-assembly, which is driven by the magnetic effect of MnS nanorods each other. Investigation on the structure and morphology of another two MnS nanocrystals obtained with further lower sulfide ion content (0.75 mmol) and with thiourea as sulfide source confirms the formation mechanism of the HS-NSs and TP-NRs nanocrystals. (**Figure S3** and detailed discussion in **ESI**)



**Figure 2**. SEM images of HS-NSs (a) and TP-NRs (b) MnS nanocrystals, (c) XRD patterns of HS-NSs and TP-NRs MnS nanocrystals, HRTEM images and FFT plots (inlets) of HS-NSs (d) and TP-NRs (e) MnS nanocrystals

It is noticed that the ratio of ammonia and sulfide ion in the hydrothermal system plays an important role in the formation of the hollow spindle-like nanospheres and tetrapod nanorods. We propose the formation mechanism of the HS-NSs and TP-NRs nanocrystals



**Scheme 1**. The formation mechanism of the HS-NSs and TP-NRs nanocrystals.

The as-prepared MnS nanocrystals with various morphologies are primary applied for supercapacitor materials and exhibit high performance. **Figure 3a** shows the CV curves of obtained various MnS nanocrystals at 2 mV s$^{-1}$. Quasi-rectangle shaped CV curves

with large wide peaks are observed in both the electrodes. This result indicates that the MnS nanocrystals are the excellent promising capacitive materials with pseudocapacitance. The specific capacitances of HS-NSs and TP-NRs MnS nanocrystals at 1 mV s$^{-1}$, calculated by calculated via **Equations S2**, are 400.6 and 704.5 F g$^{-1}$, respectively. TP-NRs MnS nanocrystals mainly with γ-phase exhibits much higher specific capacitance than the HS-NSs MnS with both α-phase and γ-phase. The higher capacitance of TP-NRs MnS nanocrystals should be ascribed to its suitable layered structure for fast electrochemical reaction as **Equations S3** and **S4**. As shown in **Figure 3e**, the α-phase is the cubic rock salt structure, while the γ-phase is metastable hexagonal wurtzite structure with layered structure between the Mn ions and the sulfide ions. When the MnS nanocrystals are electrochemically oxidized, the hydroxyl species can be easily intercalated into the layered structure constructed by the manganese ions and sulfide ions. By contrast, the resistance of this process will increase markedly for the cubic rock structure (α-phase). Therefore, more bulk active materials far from the surface of nanocrystals can be utilized to store charges, which contributes the pseudocapacitance of the MnS nanocrystals. The XRD patterns of the MnS nanocrystals at different state of charge confirms this deduction (**Figure S4** and detailed discussion in **ESI**).
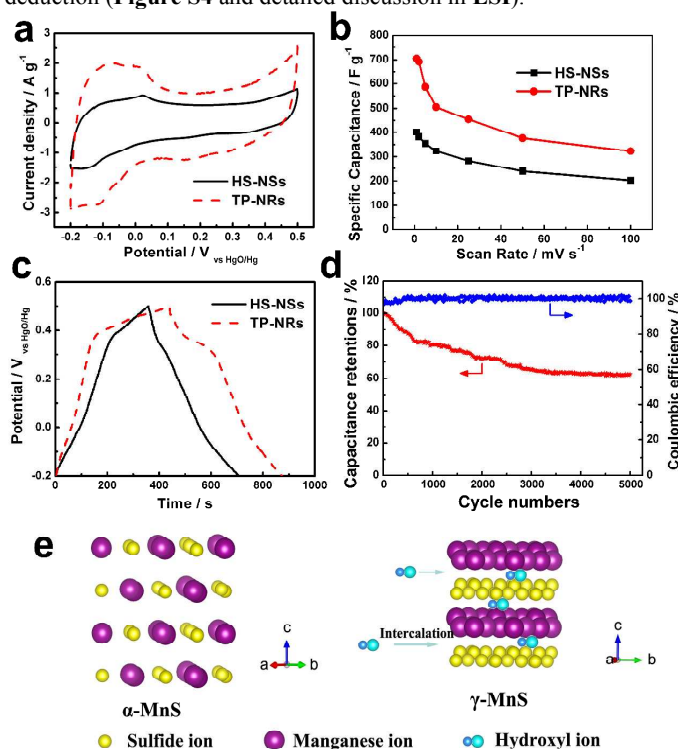
**Figure 3**. (a) CV curves of HS-NSs and TP-NRs MnS nanocrystals at 2 mV s$^{-1}$, (b) specific capacitance of HS-NSs and TP-NRs MnS nanocrystals calculated by CV curves, (c) charge-discharge curves of HS-NSs and TP-NRs MnS nanocrystals at 0.5 A g$^{-1}$, (d) life cycles of the TP-NRs MnS nanocrystals electrode, (e) structure scheme of α-MnS and γ-MnS.

The MnS TP-NRs electrode also exhibits high rate-capacity. As shown in **Figure S5a**, the regular quasi-rectangle shaped CV curve of the MnS TP-NRs electrode even in the high scan rate of 100 mV s$^{-1}$ indicates its high rate-capacity. These should be ascribed to that the interwoven porous framework, constructed by the tetrapod nanocrystals, provides suitable passages for ionic transportation and electronic conduct. **Figure 3b** shows the specific capacitance of the MnS nanocrystals calculated by CV curves at different scan rates. The specific capacitances of TP-NRs MnS nanocrystals at 1, 2, 5, 10,

25, 50, 100 mV s$^{-1}$ are 704.5, 691.8, 505.5, 454.2, 375.8 and 323.1 F g$^{-1}$, respectively. The TP-NRs MnS nanocrystals exhibit high capacitance (323.1 F g$^{-1}$) even in high scan rate (100 mV s$^{-1}$). The charge-discharge curves of MnS HS-NSs and TP-NRs are given in **Figure 3c**, sloped plateaus rather than regular triangles are observed in both electrodes, which demonstrates the pseudocapacitive characteristic of the MnS electrodes. The charge-discharge curves keep their shapes even at high current densities (**Figure S5b**), which confirms the high rate-capacity of the TP-NRs MnS electrode. Furthermore, the TP-NRs MnS electrode displays high cycle performance. As shown in **Figure 3d**, the capacity retention is 80.4 % after 1000 cycles, and even 62.6 % after 5000 cycles with high Coulombic efficiency ( > 95 %) during the whole cycles. The investigation indicates that the degradation should be mainly attributed to the phase-transfer of metastable γ-phase to stable α-phase (**Figure S6** and detailed discussion in **ESI**). Moreover, both the MnS TP-NRs and HS-NSs materials show higher specific capacitance than the $Mn_3O_4$ with solid spindle-like morphology (**Figure S7a** and **S7b**) similar to HS-NSs (**Figure S7c**), which is attributed to the higher electronic conductivity and faster charge transfer shown in EIS spectra (**Figure S7d**). Moreover, the specific capacitance of TP-NRs MnS nanocrystals is higher than those of manganese oxides reported in literatures. [22, 23]
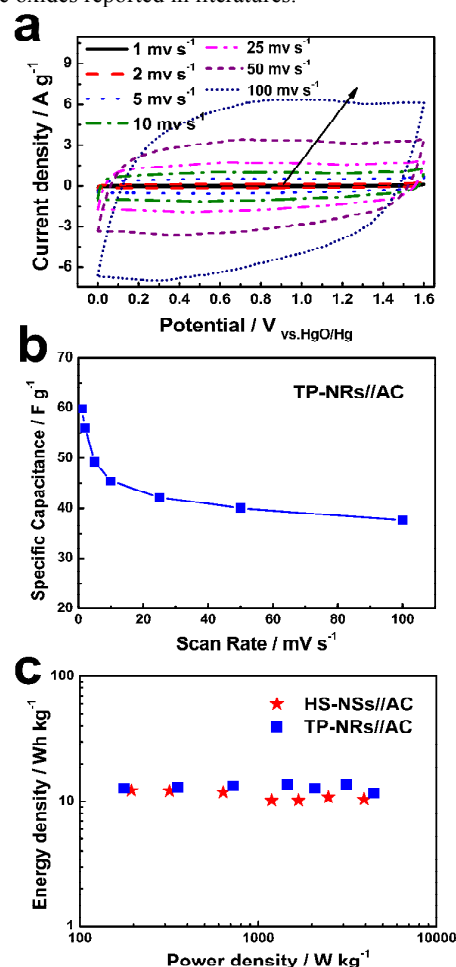
**Figure 4**. (a) CV curves at different scan rates and (b) specific capacitances at different scan rates of the as-prepared TP-NRs//AC supercapacitor, (c) Ragone plots (energy density versus power density) of the as-prepared HS-NSs//AC and TP-NRs//AC supercapacitors

Asymmetric supercapacitor with the TP-NRs MnS nanocrystals as positive material and activated carbon as the negative material

(denoted as TP-NRs//AC supercapacitor) is assembled to evaluate the practical application of the MnS nanocrystals for supercapacitor. **Figure 4a** shows the CV curves of the as-prepared TP-NRs//AC supercapacitor at different scan rates. Regular quasi-rectangle shape even at 100 mV s$^{-1}$ indicates the excellent capacitive characteristic of the TP-NRs//AC supercapacitor. The specific capacitances (calculated by the total mass of positive and negative materials) of the supercapacitor at 1, 2, 5, 10, 25, 50 and 100 mV s$^{-1}$ are 59.8, 56.1, 49.3, 45.5, 42.2, 40.0 and 37.6 F g$^{-1}$, respectively (**Figure 4b**). The capacitance retention of 62.9 % at 100 mV s$^{-1}$ indicates the high rate-capacity of the TP-NRs//AC supercapacitor. **Figure S8** shows the charge-discharge curves of TP-NRs//AC supercapacitor at different current densities. The cell voltage is as high as 1.6 V and the specific capacitance is 49.5 F g$^{-1}$ at the current of 30.4 mA, corresponding to 20 A g$^{-1}$ for positive materials. The regular triangle-shaped charge-discharge curves confirm the excellent capacitive characteristic of the supercapacitor. The energy densities versus power densities (Ragone plots) of TP-NRs supercapacitor are shown in **Figure 4c**. The energy density is 13.1 Wh kg$^{-1}$ at the power density of 70.7 W kg$^{-1}$, and 11.7 Wh kg$^{-1}$ even at the high power density of 4.45 kW kg$^{-1}$. These values are much higher than those of carbon-based symmetric supercapacitors (< 10 Wh kg$^{-1}$) in aqueous electrolytes.[24-25] The high performance of the as-prepared supercapacitor should be ascribed to the high cell voltage of the supercapacitor (1.6 V) and the high capacitance of the positive TP-NRs electrode (704.5 F g$^{-1}$). Moreover, if better negative materials are used to substitute the commercial activated carbon, the performance of the TP-NRs//AC supercapacitor will be further improved.

## Conclusions

In summery, well-defined HS-NSs and TP-NRs MnS nanocrystals are synthesized by a facile template-free hydrothermal process. The morphology and structure are easily tuned via sulfide ion content. The formation mechanism of HS-NSs and TP-NRs MnS nanocrystals is proposed and illustrated in detail. MnS nanocrystals electrodes are primary used as supercapacitor materials and exhibit high performance. The TP-NRs nanocrystals electrode with γ-phase wurtzite structure displays high specific capacitance of 704.5 F g$^{-1}$, which is higher than that of HS-NSs nanocrystals electrode, as well as manganese oxide electrode. The capacitance retention is 62.6% after 5000 cycle charge-discharge test. Asymmetric supercapacitor, assembled with the TP-NRs MnS nanocrystals as positive material, exhibits high performance. Due to the low cost and rich in natural resources of both manganese and sulfur, this work will boost the research interest of the electrochemical properties of the low-cost MnS nanocrystals and enlarge their application scales.

## Acknowledgments

## Notes and references

Hebei Key Laboratory of Applied Chemistry, College of Environmental and Chemical Engineering, Yanshan University, Qinhuangdao, Hebei, 066004, China, E-mail: tangyongfu@ysu.edu.cn

† Electronic Supplementary Information (ESI) available: [Experimental section, Supplementary equations (S1-S4), Supplementary figures (S1-S5)]. See DOI: 10.1039/c000000x/

1. Y. C. Zhang, H. Wang, B. Wang, H. Y. Xu, H. Yan, M. Yoshimura, *Opt. Mater.* **2003**, *23*, 433-437.

2. J. Lu, P. Qi, Y. Peng, Z. Meng, Z. Yang, W. Yu, Y. Qian, *Chem. Mater.* **2001**, *13*, 2169-2172.

3. X. V. Zhang, S. T. Martin, C. M. Friend, M. A. A. Schoonen, H. D. Holland, *J. Am. Chem. Soc.* **2004**, *126*, 11247-11253.

4. J. Chen, F. Cheng, *Acc. Chem. Res.* **2009**, *42*, 713-723.

5. H. Wang, L. F. Cui, Y. Yang, H. S. Casalongue, J. T. Robinson, Y. Liang, Y. Cui, H. Dai, *J. Am. Chem. Soc.* **2010**, *132*, 13978-13980.

6. H. Zhang, G. Cao, Z. Wang, Y. Yang, Z. Shi, Z. Gu, *Nano Lett.* **2008**, *8*, 2664-2668.

7. M. S. Wu, Z. S. Guo, J. J. Jow, *J. Phys. Chem. C* **2010**, *114*, 21861-21867;

8. G. Qiu, H. Huang, S. Dharmarathna, E. Benbow, L. Stafford, S. L. Suib, *Chem. Mater.* **2011**, *23*, 3892-3901;

9. L. Zhang, L. Zhou, H. B. Wu, R.Xu, X. W. Lou, *Angew. Chem. Int. Ed.* **2012**, *51*, 7267-7270.

10. N. Zhang, R. Yi, Z. Wang, R. Shi, H. Wang, G. Qiu, X. Liu, *Mater. Chem. Phys.* **2008**, *111*, 13-16.

11. G. He, C. J. Hart, X. Liang, A. Garsuch, L. F. Nazar, *ACS Appl. Mater. Interfaces* **2014**, 6, 10917-10923.

12. J. Xiao, L. Wan, S. Yang, F. Xiao, S. Wang, *Nano Lett.* **2014**, 14, 831-838.

13. H. Chen, J. Jiang, L. Zhang, H. Wan, T. Qi, D. Xia, *Nanoscale* **2013**, 5, 8879-8883.

14. Y. Zhao, Y. Zhang, H. Zhu, G. C. Hadjipanayis, J. Q. Xiao, *J. Am. Chem. Soc.* **2004**, *126*, 6874-6875.

15. J Mu, Z. Gu, L. Wang, Z. Zhang, H. Sun. S. Z. Kang, *J. Nanopart. Res.* **2008**, *10*, 197-201.

16. L. Peng, S. Shen, Y. Zhang, H. Xu, Q. Wang, *J. Colloid Interface Sci.* **2012**, 377, 13-17.

17. Y. W. Jun, Y. Y. Jung, J. Cheon, *J. Am. Chem. Soc.* **2002**, *124*, 615-619.

18. Y. Zheng, Y. Cheng , Y. Wang, L. Zhou, F. Bao, C. Jia, *J. Phys. Chem. B* **2006**, *110*, 8284-8288.

19. Y. Yan, R. M. Rioux, C. K. Erdonmez, S. Hughes, G. A. Somorjai, A. P. Alivisatos, *Science* **2004**, *304*, 711-714;

20. K. N. Tu, U. Göseleb, *Appl. Phys. Lett.* **2005**, *86*, 093111.

21. H. J. Fan, M. Knez, R. Scholz, D. Hesse, K. Nielsch, M. Zacharias, U. G. 1sele, *Nano Lett.* **2007**, *7*, 993-997.

22. S. Santhanagopalan, A. Balram, D. D. Meng, ACS Nano 2013, 7, 2114-2125.

23. H. Zhang, G. Cao, Z. Wang, Y. Yang, Z. Shi, Z. Gu, *Nano Lett.* **2008**, *8*, 2664-2668.

24. X. Huang, Z. Zeng, Z. Fan, J. Liu, H. Zhang, *Adv. Mater.* **2012**, *24*, 5979-6004.

25. L. Demarconnay, E. Ramundo-Piñero, F. Béguin, *Electrochem. Comm.* **2010**, *12*, 1275-1278